nature communications

Article

https://doi.org/10.1038/s41467-023-39002-6

Ferromagnetism emerged from non-ferromagnetic atomic crystals

Received: 11 March 2022

Accepted: 25 May 2023

Published online: 29 June 2023

Check for updates

Cheng Gong[1,2,10], Peiyao Zhang[1,3,10], Tenzin Norden[3], Quanwei Li[1], Zhen Guo[1], Apoorva Chaturvedi[4], Arman Najafi[3], Shoufeng Lan[1], Xiaoze Liu[1], Yuan Wang[1], Shi-Jing Gong[5], Hao Zeng[3], Hua Zhang[6,7,8], Athos Petrou[3] & Xiang Zhang[1,9]

The recently emerged ferromagnetic two-dimensional (2D) materials provide unique platforms for compact spintronic devices down to the atomic-thin regime; however, the prospect is hindered by the limited number of ferromagnetic 2D materials discovered with limited choices of magnetic properties. If 2D antiferromagnetism could be converted to 2D ferromagnetism, the range of 2D magnets and their potential applications would be significantly broadened. Here, we discovered emergent ferromagnetism by interfacing non-magnetic WS_2 layers with the antiferromagnetic $FePS_3$. The WS_2 exhibits an order of magnitude enhanced Zeeman effect with a saturated interfacial exchange field ~38 Tesla. Given the pristine $FePS_3$ is an intralayer antiferromagnet, the prominent interfacial exchange field suggests the formation of ferromagnetic $FePS_3$ at interface. Furthermore, the enhanced Zeeman effect in WS_2 is found to exhibit a strong WS_2-thickness dependence, highlighting the layer-tailorable interfacial exchange coupling in WS_2-$FePS_3$ heterostructures, which is potentially attributed to the thickness-dependent interfacial hybridization.

Ferromagnetic materials play foundational roles in a broad range of magnetoelectric and magneto-optical devices, including magnetoresistive memories[1], spin field effect transistors[2], and optical isolators[3]. Distinct magnetic properties prompt a wide variety of device functionalities. For example, permanent magnets with substantial energy products enable electromechanical devices, and transparent magnets with large Verdet constants enable non-reciprocal optical devices. Recently discovered magnetic atomic crystals[4–8] broaden the landscape of two-dimensional (2D) materials, provide ideal platforms for fundamental physics, and open unprecedented opportunities for ultracompact spintronic and magnonic devices. Combined with the incredible variety of 2D electronic and photonic materials, 2D magnets can significantly expand the atomic-thin magnetoelectric and magneto-optic functionalities. However, the fundamental hindrance to the prospect is the scarcity of 2D ferromagnets.

In stark contrast, antiferromagnetic van der Waals (vdW) crystals are much more abundant. Transition metal phosphorous trichalcogenides (MPX_3: M = Fe, Mn, Ni, Cd, Hg; X = S, Se) are such a family with fertile magnetic configurations such as Ising antiferromagnets $FePS_3$

[1]Nano-scale Science and Engineering Center (NSEC), 3112 Etcheverry Hall, University of California, Berkeley, CA, USA. [2]Department of Electrical and Computer Engineering and Quantum Technology Center, University of Maryland, College Park, MD, USA. [3]Department of Physics, University at Buffalo, State University of New York, Buffalo, NY, USA. [4]Center for Programmable Materials, School of Materials Science and Engineering, Nanyang Technological University, Singapore, Singapore. [5]Engineering Research Center of Nanophotonics Advanced Instrument (Ministry of Education), Department of Physics, School of Physics and Electronic Science, East China Normal University, Shanghai, China. [6]Department of Chemistry, City University of Hong Kong, Kowloon, Hong Kong, China. [7]Hong Kong Branch of National Precious Metals Material Engineering Research Center (NPMM), City University of Hong Kong, Kowloon, Hong Kong, China. [8]Shenzhen Research Institute, City University of Hong Kong, Shenzhen, China. [9]Faculties of Science and Engineering, The University of Hong Kong, Hong Kong, China. [10]These authors contributed equally: Cheng Gong, Peiyao Zhang. e-mail: xiangz@hku.hk

and $FePSe_3$[9–13], Heisenberg antiferromagnets $MnPS_3$ and $MnPSe_3$[13,14], and XY-type antiferromagnet $NiPS_3$[14]. Most compelling promises that antiferromagnets hold stem from their attractive characteristics: immunity to the environmental magnetic field perturbation because of the alternatively opposite magnetic moments, the null stray field for eliminated crosstalk between neighboring bits, and high magnetic resonance frequency for terahertz devices (in contrast to gigahertz frequency for ferromagnets) as spin reorientation in zero-magnetization antiferromagnets does not require angular momentum transfer between the spin system and external systems (e.g., the lattice). Nevertheless, the exploration of antiferromagnets confronts the intrinsic challenge of information reading due to the net vanishing magnetization. Creating 2D ferromagnetism out of vdW antiferromagnets, if could be realized, would inherently integrate the advantages of both ferromagnets and antiferromagnets (e.g., readability of ferromagnets and ultrafast switching of antiferromagnets), leading to potential breakthroughs in high-speed low-power spintronics based on atomic crystals.

Results

Here we discovered the emergent ferromagnetism from antiferromagnetic vdW crystal $FePS_3$ based on heterostructure engineering. We chose to study the heterostructure of non-magnetic WS_2 on the antiferromagnetic $FePS_3$ substrate, out of four reasons. Firstly, antiferromagnetic $FePS_3$ likely becomes a ferromagnet, for example by charge transfer doping[15,16]. Secondly, $FePS_3$ is an Ising magnet with the neighboring zigzag ferromagnetic chains antiferromagnetic coupled, whose out-of-plane oriented spin magnetic moments can couple with 2D transition metal dichalcogenides efficiently[17–19]. Thirdly, WS_2 and $FePS_3$ have similar band positions and the same chalcogen species[20,21], and therefore interfacial wavefunction may overlap efficaciously, leading to strong exchange interaction. Lastly, WS_2 is an optically active semiconductor and can act as a sensor to the nearby time-reversal symmetry breaking events[22–27]. In this heterostructure of non-ferromagnetic vdW crystals, we discovered the interfacial ferromagnetism with maximum interfacial exchange field ~38 Tesla. Our discovery of ferromagnetism from non-ferromagnetic crystals, with a giant interfacial exchange field, opens a door to creating artificial 2D ferromagnets and developing emergent 2D antiferromagnetic spintronics and valleytronics.

In this work, we synthesized bulk $FePS_3$ crystals by chemical vapor transport and applied adhesive tapes to obtain freshly cleaved surfaces of $FePS_3$ flakes on 260 nm SiO_2 on Si. Monolayer and few-layer WS_2 flakes were exfoliated on polydimethylsiloxane (PDMS). Heterostructures were prepared by direct mechanical deposition of WS_2 on the $FePS_3$-SiO_2-Si stack, as shown in Fig. 1a, b. Consistent with the literature[9–11], our bulk $FePS_3$ is an easy-axis antiferromagnet with Néel temperature at about 120 K, as shown in Fig. S1 in the supplementary information. Given the large lattice mismatch between $FePS_3$ and WS_2, we expect the effect of the interlayer registry and twist[28] if any would be averaged out, which is therefore not the focus of this work.

For single layer WS_2, two degenerate but inequivalent valleys are present at K and K′ points (neighboring corners of the hexagonal Brillouin zone). Circularly polarized photons with opposite chirality can be absorbed for the inter-band excitations at K and K′ points, respectively. For multilayer WS_2, neighboring layers have 180° relative rotation leading to the overlap of "K point of one layer" and "K′ point of the neighboring layer", hence eliminating the valley inequivalence for

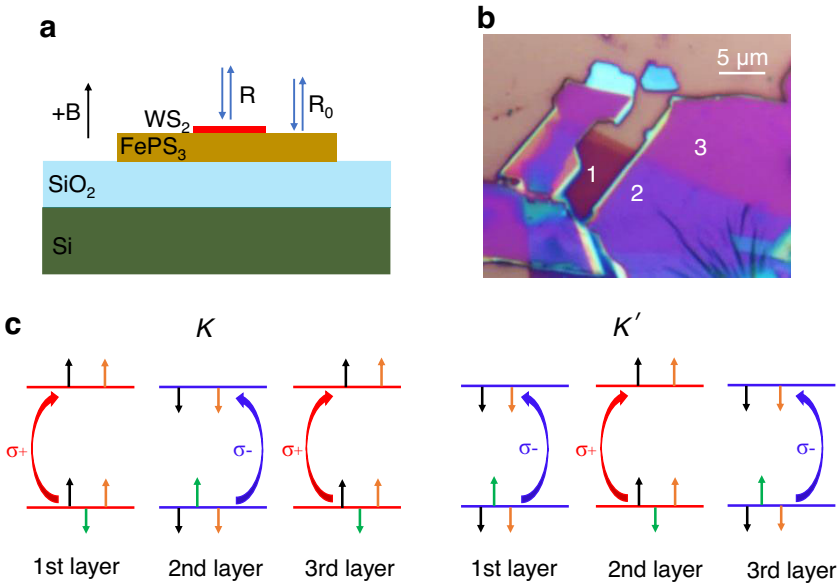

Fig. 1 | Optical image of a WS_2-$FePS_3$ heterostructure and optical selection rule of trilayer WS_2. a Side-view illustration of the WS_2-$FePS_3$ heterostructure. Circularly polarized lights are incident on the WS_2-$FePS_3$ stack and a bare $FePS_3$ flake, and reflected lights are collected as "R" and "R_0", respectively. The applied magnetic field points out-of-plane. Reflectance spectra in Fig. 2 are calculated by R/R_0. **b** An optical image of trilayer WS_2 on $FePS_3$ on the 260-nm-SiO_2/Si substrate. Numbers "1", "2", and "3" mark the regions of trilayer WS_2 on SiO_2/Si, trilayer WS_2 on $FePS_3$ on SiO_2/Si, and $FePS_3$ on SiO_2/Si. **c** The layer-resolved optical selection rule for the circularly polarized light absorption for the inter-band transition at K and K′ points of trilayer WS_2. Due to the much stronger intralayer spin orbit coupling than the interlayer coupling, the spin-valley-layer locking effect remains robust in trilayer WS_2. Left circularly polarized light is always preferentially absorbed for the inter-band excitation of spin-up polarized electrons at Brillouin zone corners, and right circularly polarized light for spin-down polarized electrons. Black, orange, and green arrows represent spin, valley, and orbital magnetic moments, respectively. Given the same spin magnetic moments of electrons at K (or K′) points of conduction and valence band edges, the external magnetic field does not change the band gap size at K (or K′) points due to its effect on spin magnetic moments. Valley magnetic moments at K (or K′) points of conduction and valence band edges could differ only if the effective mass of electrons and holes differ. Our experimental results show this difference is small. Orbital magnetic moments at K (or K′) points of conduction and valence band edges differ, as shown by the only green arrows in valence bands. Therefore, for all three layers, an external magnetic field causes the direct-gap size of the spin-up polarized bands (green arrow up) at K points to increase and that of the spin-down polarization (green arrow down) at K′ points to decrease, or vice versa. Although the photoluminescence of the multilayer WS_2 is quenched, optical reflectance spectra allow the probing of the direct-gap size at K or K′ points.

https://doi.org/10.1038/s41467-023-39002-6

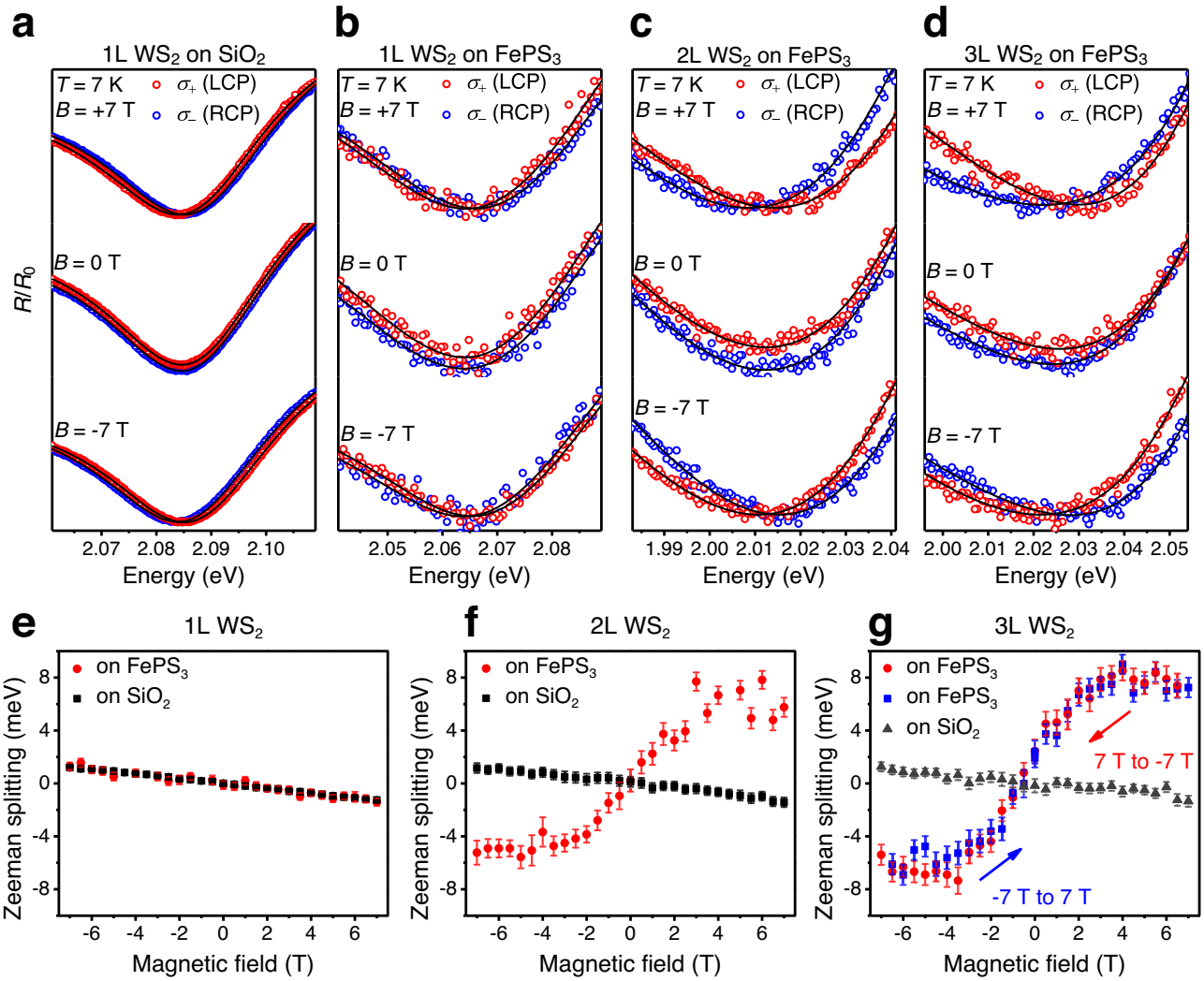

Fig. 2 | Magnetoreflectance spectra and spin splittings of monolayer, bilayer and trilayer WS_2 on $FePS_3$ and SiO_2 at 7 K. a–d Magnetoreflectance spectra of monolayer WS_2 on SiO_2 **a**, and monolayer **b**, bilayer **c**, and trilayer **d** WS_2 on thick $FePS_3$. Red and blue dots represent reflectance spectra of left and right circular polarized lights. Solid lines were fitted using a complex (absorptive plus dispersive) Fano line shape to extract the absorption transition energies. Magnetoreflectance spectra of bilayer and trilayer WS_2 on SiO_2 are presented in Figs. S3a, b. **e–g** Spin splittings of monolayer **e**, bilayer **f**, and trilayer **g** WS_2 on $FePS_3$ and on SiO_2, respectively. All different layers of WS_2 on SiO_2 exhibit the intrinsic Zeeman effect ~ −0.2 meV/T. Monolayer WS_2 on $FePS_3$ exhibit the intrinsic Zeeman effect as well. In stark contrast, bilayer and trilayer WS_2 on $FePS_3$ show an order of magnitude enhancements in lower magnetic field range −3.5 ~ 3.5 T, and saturate beyond 3.5 T. After saturation, the splitting drops slightly following the intrinsic Zeeman effect caused by external magnetic field. The "S"-shape magnetic field dependent spin splitting reveals the presence of interfacial ferromagnetism. The steeper slope in the low magnetic field range and the larger saturated spin splitting for the trilayer $WS_2/FePS_3$ heterostructure, compared with the bilayer $WS_2/FePS_3$ heterostructure, shows the stronger ferromagnetism. In **g**, the overall shift of the hysteresis loop to −0.5 ~ −1 T indicates a possible formation of an exchange bias between the ferromagnetic surface and the bulk of the antiferromagnetic $FePS_3$ substrate. Error bars arise from the uncertainty of fitted dip positions. The dip extraction of the magnetoreflectance spectra is explained in Fig. S2 and related texts in supplementary information, and the magnetoreflectance spectra of the bilayer and trilayer WS_2 on SiO_2 are shown in Fig. S3.

the even number of layers. But in fact, transition metal dichalcogenides possess unique spin-valley-layer locking effect: spin and valley remain coupled (Fig. 1c) in each constituent layer, due to the much weaker interlayer interaction than the intralayer spin orbit coupling. For all layers, left circularly polarized photons (σ +) are always preferentially absorbed to excite the inter-band transition between spin-up bands (red lines, Fig. 1c) at corners of Brillouin zone, and right circularly polarized photons (σ−) for spin-down bands (blue lines, Fig. 1c)[29,30]. Therefore, the absorption or reflectance difference of opposite circularly polarized photons by WS_2 allows the detection of the nearby time-reversal-symmetry breaking phenomena.

Figure 2a, e shows monolayer WS_2 on SiO_2 exhibits the Zeeman splitting at 7 K, linearly dependent on the externally applied magnetic field with a slope ~ −0.2 meV/T, which arises primarily from the different magnetic field responses of distinct *d*-orbital magnetic moments at conduction band edge (m_z = 0) and valence band edge (m_z = ±2) at K (or K') points[22–27,30]. For monolayer WS_2 on $FePS_3$, Zeeman splitting akin to that of WS_2 on SiO_2 was observed, which accords with the fact that antiferromagnetic $FePS_3$ has zero magnetization and thus does not enhance the Zeeman effect. Even though the antiferromagnetic $FePS_3$ and diamagnetic SiO_2 possess different magnetic susceptibility, the induced magnetic moments in both $FePS_3$ and SiO_2 are far from saturation and their dipolar effects on WS_2 are negligible. In addition, the polarized photoluminescence (PL) spectra from monolayer WS_2-$FePS_3$ show a linear magnetic field dependence of valley Zeeman splitting (Fig. S2). The slightly larger Zeeman coefficient in PL data than in reflectance data is due to the fact that the PL herein is emitted from defect states, which usually exhibit a larger g-factor than

neutral excitons[31,32]. Therefore, both PL and reflectance measurements do not show evidence of ferromagnetism in monolayer WS_2-$FePS_3$ heterostructure.

Surprisingly, still on $FePS_3$, at 7 K, bilayer WS_2 (Fig. 2c, f) exhibits a dramatically enhanced Zeeman effect. At the lower field range (e.g., −2 ~ 2 T), the spin splitting almost linearly depends on the external field with an order of magnitude larger Zeeman coefficient than the intrinsic Zeeman effect of WS_2. Given this splitting is from reflectance spectra, the unusually large g-factors of defect states[31,32] in monolayer transition metal dichalcogenides accessed by PL are ruled out. When the external magnetic field is larger than 3 T, the spin splitting saturates. Such "S"-shape field-dependence, together with its temperature-insensitivity (shown later)), rules out the giant-paramagnetic response in WS_2 when Fermi level resides at a particular point between spin-orbit-coupling split conduction bands[33,34]. Rather, it is evidence of the interfacial ferromagnetism[35,36].

To further study the effect of WS_2 thickness, we continued on a trilayer WS_2 on $FePS_3$. Similar "S"-shape magnetic field dependence of spin splitting was observed, as shown in Fig. 2g. A steeper slope and a larger saturated spin splitting were observed in the trilayer WS_2-$FePS_3$, with respect to the bilayer WS_2-$FePS_3$. The saturated splittings for the bilayer and trilayer WS_2 are about 5.5 meV and 7.5 meV, respectively, when the external magnetic field amounts to ~3.5 T in both cases. Under the external magnetic fields higher than 3.5 T, the magnitude of the spin splitting reduces slightly following the intrinsic Zeeman effect ~ −0.2 meV/T. The opposite sign of the enhanced Zeeman effect (due to magnetic proximity effect) with respect to the intrinsic Zeeman effect could relate to the specific interfacial magnetic coupling (e.g., antiferromagnetic interfacial proximity effect[37] between ferromagnetic $FePS_3$ surface and WS_2), which again highlights the fundamental difference between magnetic proximity effect and Zeeman effect. The negligible opening in the hysteresis loops for both bilayer and trilayer WS_2-$FePS_3$ exhibit the small remanence which may result from many small-size domains that cannot be resolved by our optical approach.

Regarding the effect of WS_2 thickness on the interfacial ferromagnetism, we deemed two mechanisms are possible. Firstly, the thicker WS_2 with a narrower band gap has the conduction band edge closer to that of $FePS_3$[20,21], leading to the more effective wavefunction overlap of the two materials and their exchange interaction. Such interfacial hybridization is ubiquitous, orbital-dependent, and could effectively alter the magnetic properties[38,39]. Our density functional theory (DFT) calculation of WS_2-$FePS_3$ heterostructures confirms the orbital-dependent charge redistribution within $FePS_3$ (Figs. S5 and S6) evolves with the WS_2 thickness, indicating the interfacial hybridization sensitively depends on the WS_2 thickness. Such interfacial hybridization likely causes band renormalization in WS_2, leading to the anomalous WS_2 thickness dependent reflectance dip positions (Fig. 2b–d: monolayer, 2.065 eV; bilayer, 2.015 eV; trilayer, 2.028 eV) on $FePS_3$ substrate. Secondly, charge transfer between WS_2 and $FePS_3$ could partially participate in triggering the magnetic phase change of the $FePS_3$ surface from antiferromagnetism to ferromagnetism. However, our DFT calculations indicate the role of charge transfer if any would be secondary, as the amount of interfacial charge transfer is not significant enough for a magnetic phase change[40] (see discussions in supplementary information).

The saturated exchange fields between $FePS_3$ and the bilayer and trilayer WS_2 are about 28 and 38 Tesla, respectively. Considering the measured splitting is an average result from multiple WS_2 layers, the exchange fields between the very interfacial layer of WS_2 and $FePS_3$ can be even stronger. The giant interfacial exchange field strengths are roughly three times of that in previously studied WSe_2/EuS, WSe_2/CrI_3, and graphene/EuS systems[36,41,42], and of the same order as the exchange field strengths observed in WS_2/EuS heterostructures[37]. The interfacial exchange interaction depends on the specific wavefunction overlap between the two materials, and becomes especially strong when the interfacial interaction is mediated by the same species (such as in WS_2/EuS)[37]. As analyzed above, the close band positions and the same chalcogen species of WS_2 and $FePS_3$, could be important factors for the observed giant interfacial exchange field. To confirm the role of the same interfacial chalcogen species in the resultant interfacial ferromagnetism, we conducted the systematic control experiments on monolayer, bilayer and trilayer WSe_2 on $FePS_3$, and monolayer, bilayer and trilayer WS_2 on $FePSe_3$, respectively (the chalcogen species in the two constituent materials of these heterostructures are different). As shown in Fig. S7, all the studied WSe_2/$FePS_3$ and WS_2/$FePSe_3$ samples do not exhibit interfacial ferromagnetism as the WS_2/$FePS_3$ samples do. This delivers strong evidence for the role of the chalcogen mediated interfacial hybridization in the resultant interfacial ferromagnetism.

The temperature dependent study further confirms the correlation between the ferromagnetic surface and the antiferromagnetic substrate. For both bilayer and trilayer WS_2-$FePS_3$ heterostructures, the magnetic field-dependent spin splittings at 80 K agree well with that at 7 K, which implicates the application prospects above liquid nitrogen temperature. Under a fixed 5 T external field, when temperatures are elevated above 120 K, the enhanced Zeeman effect suddenly disappears and the spin splitting restores to the intrinsic values (~−1 meV at 5 T). The coincidence of the Curie temperature of the interface ferromagnetism with the Néel temperature of the antiferromagnetic $FePS_3$ substrate confirms the origin of the observed ferromagnetism from the $FePS_3$ surface. At 130 K, the magnetic field dependences of the spin splittings in bilayer and trilayer WS_2 in heterostructures resemble the behaviors of their counterparts on SiO_2 at 7 K, in both magnitude and sign, except the larger noise arising from the stronger thermal smearing of the spin-polarized bands at elevated temperatures.

The spin splittings in bilayer WS_2-$FePS_3$ almost stay constant below and decay abruptly at 120 K, but that in trilayer WS_2-$FePS_3$ decay gradually below 120 K, as shown in Fig. 3a, d. This is similar to the temperature dependent magnetization behaviors of the conventional ferromagnetic materials: under a lower magnetic field, magnetization barely changes below and abruptly drops at the transition temperature, but under a higher magnetic field, magnetization drops continuously as temperature elevates to the transition temperature (1). This behavior relates to the thermal stability of the magnetostatic energy: under a larger magnetic field, a ferromagnet has fewer domains with stronger dipolar interaction and higher magnetostatic energy; the thermal instability of the large magnetic dipolar interaction causes the gradual temperature evolution of magnetization. Our trilayer WS_2-$FePS_3$ system exhibits a stronger interfacial magnetization compared with the bilayer WS_2-$FePS_3$ system, and therefore shows a stronger temperature evolution.

In summary, the interfacial ferromagnetism is created by laying the bilayer and trilayer WS_2 over the Ising antiferromagnet $FePS_3$. Giant interfacial exchange fields enable an order of magnitude enhanced Zeeman effect in the excitonic feature of WS_2 in WS_2/$FePS_3$ heterostructures. The high Néel temperature of antiferromagnetic $FePS_3$ sustains the high temperature ferromagnetic phase at the interface. The discovery of such a ferromagnetism emerged from non-ferromagnetic atomic crystals, with giant interfacial exchange fields, opens the door to activating layered antiferromagnets. The inherent integration of the antiferromagnet, strong spin-orbit coupling material and the emergent interfacial ferromagnet in this new heterostructure platform opens up new possibilities to harness emergent ferromagnetism for spintronic, valleytronic, and optoelectronic devices.

Methods

Growth of bulk $FePS_3$ crystal

For the single crystal chemical vapor transport (CVT) growth, the stoichiometric amounts of iron powder (Aldrich, >99%), red phosphorus lump (Alfa Aesar, Puratronic®, 99.999 + % (metal basis)), and

https://doi.org/10.1038/s41467-023-39002-6

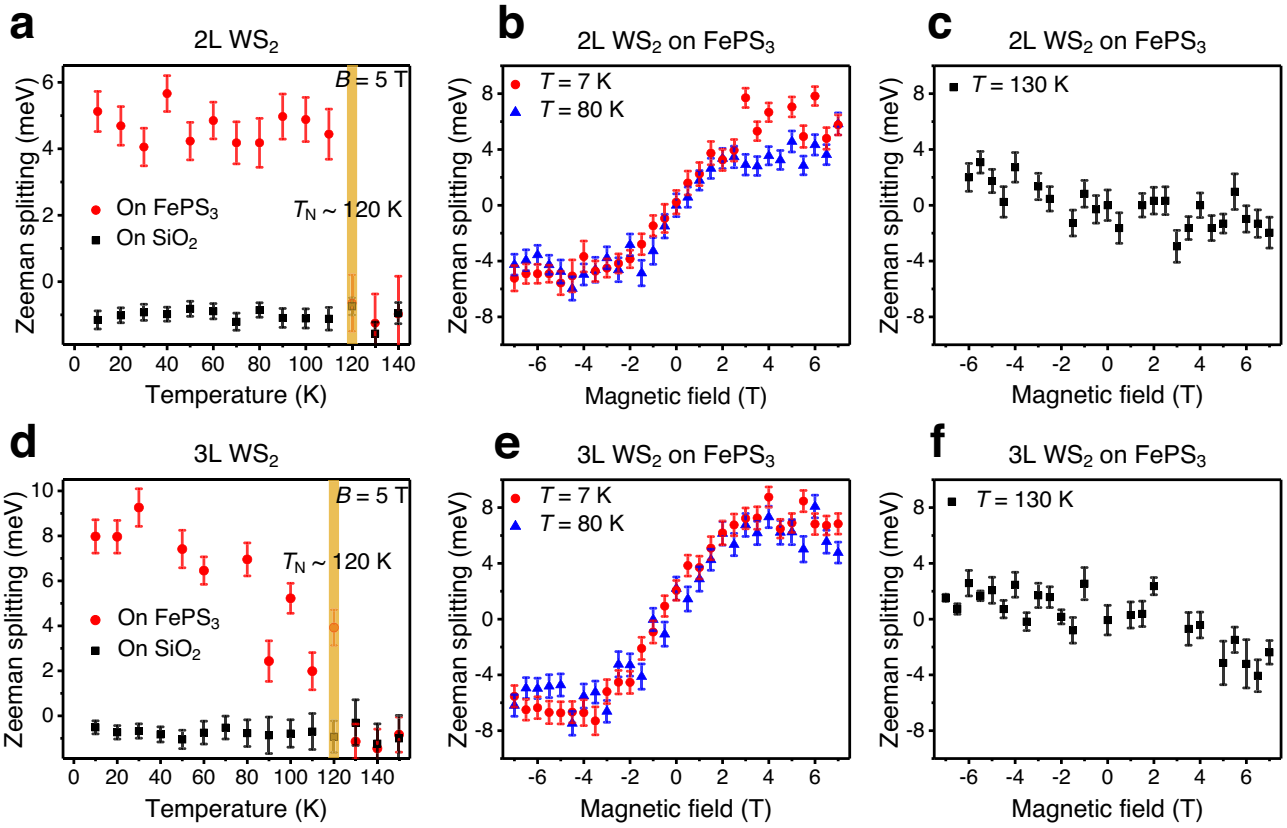

Fig. 3 | Temperature dependence of the enhanced Zeeman effects in $WS_2/FePS_3$ heterostructures. a, **d** Temperature dependent spin splitting for the bilayer **a** and trilayer **d** WS_2 on $FePS_3$ (versus on SiO_2 as a reference), under 5 T magnetic field. Below 120 K, the spin splitting for WS_2 on $FePS_3$ is drastically enhanced. Above 120 K, spin splitting for WS_2 on $FePS_3$ restores to the intrinsic Zeeman splitting as on SiO_2. **b**, **e** Magnetic field dependent spin splitting for the bilayer **b** and trilayer **e** WS_2 on $FePS_3$ at 7 K and 80 K, respectively. For both bilayer and trilayer WS_2 on $FePS_3$, the enhanced Zeeman effects do not show a notable difference between 7 K and 80 K, implicating the application potentials above liquid nitrogen temperature. **c**, **f** Magnetic field dependent spin splitting for the bilayer **c** and trilayer **f** WS_2 on $FePS_3$ at 130 K. Above Néel temperature (~ 120 K) of the $FePS_3$ substrate, the previously observed enhanced Zeeman effects disappear. The large noise in (**c** and **f**) compared with the intrinsic Zeeman effect at the lower temperature (e.g., Fig. 2f, g) is due to the thermal smearing of the spin-polarized bands at elevated temperatures. Error bars in **a**–**f** represent the uncertainty of the fitted reflectance dip positions.

sulfur pieces (Alfa Aesar, Puratronic®, 99.9995% (metal basis)) were used. These chemicals were used as-received without further purification. The materials were sealed in an evacuated quartz tube (ampoule) with an inner pressure in the range of 10^{-5} Torr to 10^{-6} Torr. In addition to the elemental constituents (Fe, P, and S), a small amount (2 mg/cc) of iodine spheres were added inside the ampoule to act as the transport agent. Sealed ampoules were then subjected to a two-zone horizontal tube furnace.

Initially, the source zone was kept at 650 °C and the growth zone at 750 °C for 48 h. This was done to allow the constituents to react completely as well as prevent the back transport or formation of undesired additional phases. After this duration, the temperature of the source zone was gradually increased to 750 °C and that of the growth zone was lowered to 700 °C. This arrangement continued for the next 120 h. Further, the temperatures of both the zones were lowered down, and the plate-like crystals were subsequently obtained from the ampoule for further characterizations and measurements.

WS_2-$FePS_3$ heterostructure assembling

The WS_2 bulk crystals and polydimethylsiloxane (PDMS) films were purchased from HQ Graphene and Gel-Pak, respectively. After the few-layer WS_2 was exfoliated on PDMS films, the WS_2-PDMS-glass slide stack was mounted to a translation stage, and moved under an optical microscope to be matched onto the exfoliated $FePS_3$ flake on the 260 nm SiO_2/Si chip. After lifting up the glass slide, the PDMS film was lifted up leaving the few-layer WS_2 on $FePS_3$ on SiO_2/Si. Overnight annealing of the samples in high vacuum (<10^{-8} torr) at 150 °C was done before loading the samples to the cryostat for the systematic magnetoreflectance study.

Magnetoreflectance measurements

The samples were placed on the cold finger of a continuous-flow optical cryostat operated in the 5–300 K temperature range. The cryostat was mounted on a three-axis translator with a spatial resolution of 10 μm in each direction. The cryostat tail was positioned inside the room temperature bore of a 7 T superconducting magnet. A collimated white-light beam was used for the reflectivity work. The incident light was focused on the sample using a microscope objective with a working distance of 34 mm. The incident beam was polarized either as left circular polarization (σ_+) or right circular polarization (σ_-) using a Babinet-Soleil compensator. The objective collected the reflected beam from the sample in the Faraday geometry and the light was focused onto the entrance slit of a single monochromator that uses a cooled charge-coupled device detector array.

Density functional theory (DFT) calculations

First-principles calculations based on the DFT were performed by using the projector augmented wave (PAW) method implemented in Vienna Ab-initio Simulation Package (VASP)[43]. Generalized gradient approximation (GGA) in the scheme of Perdew-Burke-Ernzerhof (PBE) was used to treat the exchange-correlation potential[44]. The structures were relaxed until the Hellmann-Feynman forces on each atom are less

than 0.01 eV/Å. The thickness of the vacuum region along the z axis is 15 Å. The van der Waals correction (vdW-DF) was adopted to optimize the lattice structures and bond lengths. For the Hubbard-U term[45], Dudarev's approach was used to treat localized *d* orbitals in Fe, using the effective U parameter of $U_{eff} = 2$ eV. The energy cutoff of 500 eV for the plane wave expansion and a $7 \times 7 \times 1$ k-point grid were used for the self-consistent calculations, and the total energy was converged within 1×10^{-5} eV. The in-plane lattice constant for $FePS_3$ $2 \times 2 \times 1$ supercell is 11.894 Å, and the in-plane lattice parameter for WS_2 $4 \times 4 \times 1$ supercell is 12.732 Å, which leads to a mismatch of ~6.6% between the $FePS_3$ and WS_2 supercell.

Data availability

The authors declare that the data supporting the findings of this study are available within the paper and its supplementary information files. Additional information is available from the corresponding author upon reasonable request.

Code availability

The data analysis computer codes used in this study are available from the corresponding author upon reasonable request.

References

1. Chappert, C., Fert, A. & Van Dau, F. N. The emergence of spin electronics in data storage. *Nat. Mater.* **6**, 813–823 (2007).
2. Datta, S. How we proposed the spin transistor. *Nat. Electron.* **1**, 604 (2018).
3. Bi, L. et al. On-chip optical isolation in monolithically integrated non-reciprocal optical resonators. *Nat. Photon.* **5**, 758–762 (2011).
4. Gong, C. et al. Discovery of intrinsic ferromagnetism in two-dimensional van der Waals crystals. *Nature* **546**, 265–269 (2017).
5. Huang, B. et al. Layer-dependent ferromagnetism in a van der Waals crystal down to the monolayer limit. *Nature* **546**, 270–273 (2017).
6. Gong, C. & Zhang, X. Two-dimensional magnetic crystals and emergent heterostructure devices. *Science* **363**, eaav4450 (2019).
7. Burch, K. S., Mandrus, D. & Park, J.-G. Magnetism in two-dimensional van der Waals materials. *Nature* **563**, 47–52 (2018).
8. Gibertini, M., Koperski, M., Morpurgo, A. F. & Novoselov, K. S. Magnetic 2D materials and heterostructures. *Nat. Nanotechnol.* **14**, 408–419 (2019).
9. Lee, J.-U. et al. Ising-type magnetic ordering in atomically thin $FePS_3$. *Nano Lett.* **16**, 7433–7438 (2018).
10. Klingen, V. W., Eulenberger, G. & Hahn, H. Uber die Darstellung und Eigenschaften von Hexathio- und Hexaselenohypodiphosphaten. *Z. Anorg. Allg. Chem.* **401**, 97–112 (1973).
11. Wildes, A. R., Rule, K. C., Bewley, R. I., Enderle, M. & Hicks, T. J. The magnon dynamics and spin exchange parameters of $FePS_3$. *J. Phys.: Condens. Matter* **24**, 416004 (2012).
12. Taylor, B., Steger, J., Wold, A. & Kostiner, E. Preparation and properties of iron phosphorus triselenide, $FePSe_3$. E. *Inorg. Chem.* **13**, 2719–2721 (1974).
13. Wiedenmann, A., Rossat-Mignod, J., Louisy, A., Brec, R. & Rouxel, J. Neutron diffraction study of the layered compounds $MnPSe_3$ and $FePSe_3$. *Solid State Commun.* **40**, 1067–1072 (1981).
14. Joy, P. A. & Vasudevan, S. Magnetism in the layered transition-metal thiophosphates MPS_3 (M=Mn, Fe, and Ni). *Phys. Rev. B* **46**, 5425–5433 (1992).
15. Léaustic, A. et al. High-T_C magnets in a series of substituted pyridinium-$FePS_3$ layered intercalates. *Chem. Mater.* **8**, 1954–1961 (1996).
16. Li, X., Wu, X. & Yang, J. Half-metallicity in $MnPSe_3$ exfoliated nanosheet with carrier doping. *J. Am. Chem. Soc.* **136**, 11065–11069 (2014).
17. Cao, T. et al. Valley-selective circular dichroism of monolayer molybdenum disulphide. *Nat. Commun.* **3**, 887 (2002).
18. Zeng, H., Dai, J., Yao, W., Xiao, D. & Cui, X. Valley polarization in MoS_2 monolayers by optical pumping. *Nat. Nanotechnol.* **7**, 490–493 (2012).
19. Mak, K. F., He, K., Shan, J. & Heinz, T. F. Control of valley polarization in monolayer MoS_2 by optical helicity. *Nat. Nanotechnol.* **7**, 494–498 (2012).
20. Zhang, X., Zhao, X., Wu, D., Jing, Y. & Zhou, Z. $MnPSe_3$ monolayer: a promising 2D visible-light photohydrolytic catalyst with high carrier mobility. *Adv. Sci.* **3**, 1600062 (2016).
21. Gong, C. et al. Band alignment of two-dimensional transition metal dichalcogenides: Application in tunnel field effect transistors. *Appl. Phys. Lett.* **103**, 053513 (2013).
22. Li, Y. et al. Valley splitting and polarization by the Zeeman effect in monolayer $MoSe_2$. *Phys. Rev. Lett.* **113**, 266804 (2014).
23. Srivastava, A. et al. Valley Zeeman effect in elementary optical excitations of monolayer WSe_2. *Nat. Phys.* **11**, 141–147 (2015).
24. Aivazian, G. et al. Magnetic control of valley pseudospin in monolayer WSe_2. *Nat. Phys.* **11**, 148–152 (2015).
25. MacNeill, D. et al. Breaking of valley degeneracy by magnetic field in monolayer $MoSe_2$. *Phys. Rev. Lett.* **114**, 037401 (2015).
26. Mitioglu, A. A. et al. Optical investigation of monolayer and bulk tungsten diselenide (WSe_2) in high magnetic fields. *Nano Lett.* **15**, 4387–4392 (2015).
27. Stier, A. V., McCreary, K. M., Jonker, B. T., Kono, J. & Crooker, S. A. Exciton diamagnetic shifts and valley Zeeman effects in monolayer WS_2 and MoS_2 to 65 Tesla. *Nat. Commun.* **7**, 10643 (2016).
28. Zollner, K., Faria Junior, P. E. & Fabian, J. Proximity exchange effects in $MoSe_2$ and WSe_2 heterostructures with CrI_3: Twist angle, layer, and gate dependence. *Phys. Rev. B* **100**, 085128 (2019).
29. Zhu, B., Zeng, H., Dai, J., Gong, Z. & Cui, X. Anomalously robust valley polarization and valley coherence in bilayer WS_2. *Proc. Natl Acad. Sci.* **111**, 11606–11611 (2014).
30. Jiang, C. et al. Zeeman splitting via spin-valley-layer coupling in bilayer $MoTe_2$. *Nat. Commun.* **8**, 802 (2017).
31. Srivastava, A. et al. Optically active quantum dots in monolayer WSe_2. *Nat. Nanotechnol.* **10**, 491–496 (2015).
32. Koperski, M. et al. Single photon emitters in exfoliated WSe_2 structures. *Nat. Nanotechnol.* **10**, 503–506 (2015).
33. Back, P. et al. Giant Paramagnetism-induced valley polarization of electrons in charge-tunable monolayer $MoSe_2$. *Phys. Rev. Lett.* **118**, 237404 (2017).
34. Wang, Z., Mak, K. F. & Shan, J. Strongly interaction-enhanced valley magnetic response in monolayer WSe_2. *Phys. Rev. Lett.* **120**, 066402 (2018).
35. Wang, Z., Tang, C., Sachs, R., Barlas, Y. & Shi, J. Proximity-induced ferromagnetism in graphene revealed by the anomalous hall effect. *Phys. Rev. Lett.* **114**, 016603 (2015).
36. Zhao, C. et al. Enhanced valley splitting in monolayer WSe_2 due to magnetic exchange field. *Nat. Nanotechnol.* **12**, 757–762 (2017).
37. Norden, T. et al. Giant valley splitting in monolayer WS_2 by magnetic proximity effect. *Nat. Commun.* **10**, 4163 (2019).
38. Žutić, I., Matos-Abiague, A., Scharf, B., Dery, H. & Belashchenko, K. Proximitized materials. *Mater. Today* **22**, 85–107 (2019).
39. Yang, H. et al. Significant Dzyaloshinskii–Moriya interaction at graphene-ferromagnet interfaces due to the Rashba effect. *Nat. Mater.* **17**, 605–609 (2018).
40. Chittari, B. L. et al. Electronic and magnetic properties of single-layer MPX_3 metal phosphorous trichalcogenides. *Phys. Rev. B* **94**, 184428 (2016).
41. Zhong, D. et al. Van der Waals engineering of ferromagnetic semiconductor heterostructures for spin and valleytronics. *Sci. Adv.* **3**, e1603113 (2017).
42. Wei, P. et al. Strong interfacial exchange field in the graphene/EuS heterostructure. *Nat. Mater.* **15**, 711–716 (2016).

43. Kresse, G. & Furthmuller, J. Efficient iterative schemes for ab initio total-energy calculations using a plane-wave basis set. *Phys. Rev. B* **54**, 11169–11186 (1996).
44. Perdew, J. P., Burke, K. & Ernzerhof, M. Generalized gradient approximation made simple. *Phys. Rev. Lett.* **77**, 3865 (1996).
45. Dudarev, S. L., Botton, G. A., Savrasov, S. Y., Humphreys, C. J. & Sutton, A. P. Electron-energy-loss spectra and the structural stability of nickel oxide: an LSDA+U study. *Phys. Rev. B* **57**, 1505–1509 (1998).

Acknowledgements

C.G., P.Z., Q.L., S.L., X.L. Y.W., and X.Z. acknowledge the support of the Gordon and Betty Moore Foundation (award no. 5722) and the Ernest S. Kuh Endowed Chair Professorship. C.G. acknowledges the support from the Air Force Office of Scientific Research under award no. FA9550-22-1-0349. S.-J.G. acknowledge the support from the National Natural Science Foundation of China with award no. 62274066.

Author contributions

C.G. and X.Z. conceived the project and designed the experiments. C.G. prepared heterostructure samples with the assistance of P.Z. and Z.G. C.G., X.L., and Q.L. conducted initial optical characterizations of the heterostructures. P.Z. and T.N. conducted magneto-optical reflectance measurements with the assistance of A.N. and C.G. under the supervision of A.P. and X.Z. A.C. synthesized $FePS_3$ bulk crystals under the supervision of H. Zhang. S.-J.G. conducted the DFT calculations with the discussions with C.G. X.Z. supervised the project, and C.G. wrote the manuscript assisted by P.Z. C.G., P.Z., A.P., and X.Z. analyzed the experimental results with discussions with S.L., Y.W., and H. Zeng. All authors commented on the manuscript.

Competing interests

The authors declare no competing interests.

Additional information

Supplementary information The online version contains supplementary material available at https://doi.org/10.1038/s41467-023-39002-6.

Correspondence and requests for materials should be addressed to Xiang Zhang.

Peer review information *Nature Communications* thanks the anonymous reviewer(s) for their contribution to the peer review of this work.